Pseudospin-dependent *Zitterbewegung* in monolayer graphene

Eduardo Serna, I. Rodríguez Vargas, R. Pérez-Álvarez, and L. Diago-Cisneros [iD]
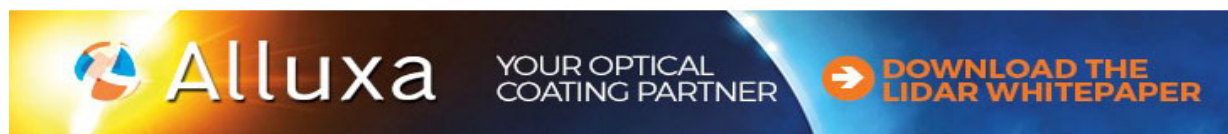
View Online   Export Citation   CrossMark

Pseudospin-dependent *Zitterbewegung* in monolayer graphene

Eduardo Serna,[1,a)] I. Rodríguez Vargas,[2,b)] R. Pérez-Álvarez,[3,c)] and L. Diago-Cisneros[1,4,d)] (iD)

AFFILIATIONS

[1] Dep. de Física y Matemáticas, Universidad Iberoamericana, Ciudad de México, CDMX 01219, Mexico
[2] Unidad Académica de Física, Univ. Autónoma de Zacatecas, Zacatecas 98060, Mexico
[3] Centro de Investigación en Ciencias, Universidad Autónoma del Estado de Morelos, Cuernavaca 62209, Mexico
[4] Facultad de Física, Universidad de La Habana, La Habana 10400, Cuba

[a)] Electronic mail: sernaed95@gmail.com
[b)] Electronic mail: isaac@fisica.uaz.edu.mx
[c)] Electronic mail: rpa@uaem.mx
[d)] Author to whom correspondence should be addressed: ldiago@fisica.uh.cu

ABSTRACT

We propose a spintronic device based on a narrow nanoribbon patterned from a monolayer graphene (MLG) sheet, embedded between a film of hexagonal boron nitride and a SiO_2 substrate, all comprised under a three top-gated structure, to explore spin-dependent quantum transport of Dirac fermions. We developed a theoretical procedure for describing the pseudospin-related effects and the dynamics of Dirac fermions represented by a one-dimensional Gaussian wave packet (1DGWP), which is electrostatically confined in the device. The free-space 1DGWP time evolution follows expected features. Meanwhile, due to the weak breakdown of the real-spin degeneracy, the 1DGWP barely splits inside the under-barrier region governed by the extrinsic Rashba spin–orbit interaction (SOI-R). Most importantly, departing from the pristine MLG, we have found evidence of trembling antiphase oscillations in the probability density time-distribution for each sublattice state, which we have called the pseudospinorial *Zitterbewegung* effect (PZBE). The PZBE appears modulated with robust transient character and with a decay time in the femtosecond scale. Interestingly, several features of the PZBE become tunable, even its complete disappearance at the vicinity of the Dirac points or at a symmetric pseudospin configuration. For the proposed quasi-1D MLG device, we have captured evidence of the familiar Klein tunneling and the unusual anti-Klein tunneling, whose interplay for 2D MLG under tunable SOI-R was reported recently.

I. INTRODUCTION

In the last few decades, graphene has been shown to be a material with very useful properties for spintronics. Intensive studies were addressed to this topic, looking for the miniaturization of, as well as for the improvement in the efficiency of, graphene-based devices, taking advantage of the material's low-energy excitation[1] and better energetic exploitation.[2] Other intriguing characteristics of graphene are its chirality, gapless spectrum, and spin-charge carriers that mimic massless relativistic particles called Dirac fermions.[3–5]

Since the early elucidation by Schrödinger,[6] back in the age of the rise of quantum mechanics, the free-space relativistic-electron "trembling motion" is still one of the relevant anomalous phenomena

present in solid materials, and being somewhat puzzling, remains yet cryptic to detect experimentally. According to Schrödinger, the relativistic-electron position experiences rapid periodic oscillations, which he called the *Zitterbewegung* effect (ZBE). However, years later, several aspects were reexamined by Dirac[7] and the average quantities over the Compton scale had to be invoked to recover meaningful results.[8,9] On the contrary, it has been demonstrated that relativistic-electron spatial localization can be narrower than the Compton wavelength, together with the lack of any ZBE, because the pair $e^- - e^+$ interaction is forbidden by the relativistic quantum-field theory.[10] These outstanding pioneering works[6,7] have inspired a large number of theoretical studies in different physical systems, for instance, in semiconductors[11,12] (and the
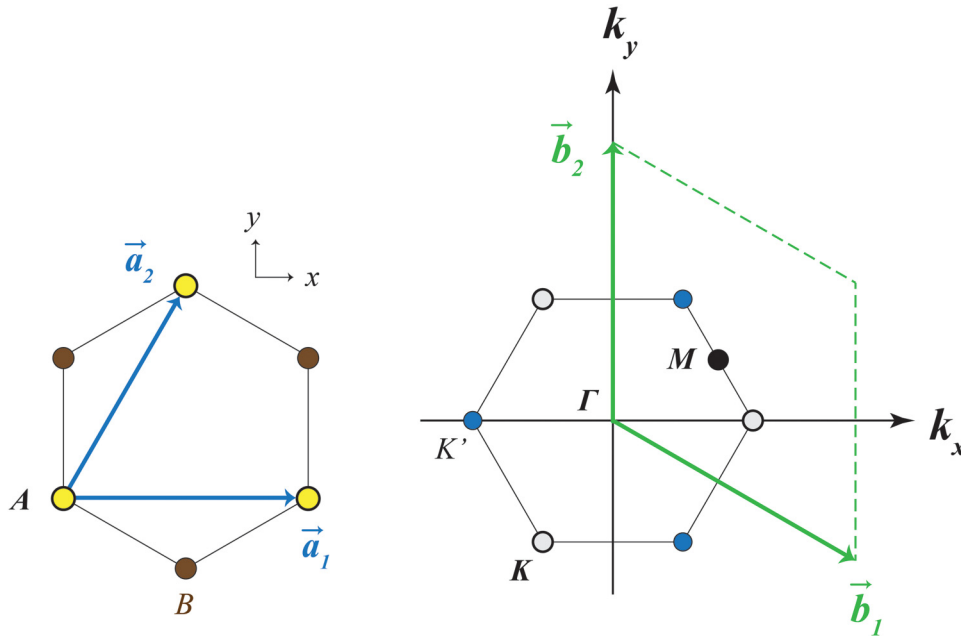
FIG. 1. Monolayer graphene lattice and its Brillouin Zone. Left panel: the sublattice sites for atoms A and B, whereas $\vec{a}_1$ and $\vec{a}_2$ are the lattice unit vectors. Right panel: a standardized view for the Brillouin Zone. Dirac's points $K(K')$ allocation is referred to the high-symmetry Γ point, whose coordinates are $k_x = \pm(4\pi/3a_0)$ and $k_y = 0$.

references therein), and in graphene,[1,8,13,14] pursuing a deeper insight into the experimentally evasive ZBE.

Several low-dimensional materials such as silicene, germanene, and dichalcogenides seem more promising than graphene in demonstrating spin–orbit effects, mostly due to their spectrum properties at the vicinity of high symmetry points.[2] Thus, creating a strong Rashba spin–orbit interaction (SOI-R) in graphene is universally agreed as a challenging task. Nevertheless, a lot of effort has gone into developing reliable routes to spin-dependent appliances in aspects other than the enhanced SOI-R strength.[2,3] For example, by testing the existence of spin-orbit coupling (SOC) in graphene, it was demonstrated that the material had an extremely weak SOC with the absence of hyperfine interaction.[3] The authors concluded that these properties turn graphene into an excellent if not an ideal material for spin-*qbits* and in this way guarantee reliable graphene-based quantum computing.[3] Meanwhile, this and other related questions have also been reviewed in other studies,[2,15,16] which reproduced similar features for the SOI-R, which makes graphene a very good candidate to be used in the management of *qbits*. Besides, there is a belief that there could exist an interplay between the ZBE and the SOI-R,[9] following the dependence of the ZBE on the strength of SOI-R in III–V semiconducting quantum wells.

We get motivated by the mere fact that somewhat exotic quantum electrodynamics (QED) phenomena such as the Klein (anti-Klein) tunneling and the ZBE—which cannot be observable for nonrelativistic particles—could arise in such nonstandard geometry as the one sketched in Fig. 2 for a monolayer graphene (MLG) nanoribbon. In this context, our theoretical approach for describing quasi-one-dimensional (Q1D) Dirac fermions' quantum motion in the envisioned device could contribute to a better understanding of the pseudospinorial *Zitterbewegung* effect

(PZBE) that we have found and of the other pseudospin-related properties of the Q1D MLG. This is the main purpose of the present study. We hope that this attempt would be scientifically sound enough to generate interest, from both the fundamental and the technological standpoints. As a collateral goal, we would like to focus on the question whether a weak SOI-R creates any benchmark when the Q1D Dirac fermions interact with a quantum potential barrier (QB).

The remaining part of this paper is organized as follows: Sec. II presents the physical model under study regarding the proposed device structure. Section III explains briefly the theoretical approach and the mathematical tools to solve it. Further numerical results are discussed in Sec. IV. Finally, in Sec. V, we sum up.

II. PHYSICAL MODEL

The MLG is composed by a semiflat single-carbon-atom sheet, with a honeycomblike lattice (see Fig. 1). The specific MLG structure, which fairly reproduces the envisioned system of the present study, is depicted in Fig. 1 and can be described by a triangular lattice with a basis of two atoms per unit cell. Accordingly, the unit-cell vectors are $\vec{a}_1 = a_0(1, 0)$ and $\vec{a}_2 = a_0/2(1, \sqrt{3})$,[4] which generate the unit-cell vectors of the Brillouin Zone (BZ) that are given by $\vec{b}_1 = 4\pi/(2a_0\sqrt{3})(\sqrt{3}, -1)$ and $\vec{b}_2 = 4\pi/(a_0\sqrt{3})(0, 1)$, with $a_0 = \sqrt{3}a$, where $a \approx 1.42\,\text{Å}$ is the carbon–carbon distance. From the BZ represented in Fig. 1, we can find Dirac's points allocated at the following (k_x, k_y) pair coordinates of the reciprocal lattice: $K = (0, 0)$; and $K' = \pm(8\pi/3a_0, 0)$.

The most common and reliable configuration for device setups, based upon two-dimensional (2D) MLG, few-layers graphebe (FLG), and nanotubes, is made with an insulating SiO_2

substrate often attached to a silicon wafer.[17-19] What the experiments have shown unequivocally is that although the 2D MLG primarily follows the underlying morphology of SiO₂, the graphene sheet due to its intrinsic stiffness does not become completely conformed to the substrate.[17] On the other hand, it has been recently reported that the hexagonal boron nitride (hBN) matches with graphene better than other candidates because of a lattice mismatch of only 1.5% between them, thus allowing graphene to preserve its morphological, optical, and electronic properties.[20]

Figure 2 shows the schematic setup of the spintronic device that we introduced as the envisioned physical system to be studied in the present work. The device's Q1D quantum channel is a narrow nanoribbon (middle yellow strip) lithographically patterned from a 2D MLG sheet (red), embedded between a film of hBN (transparent gray) and a SiO₂ substrate (green), all comprised under a three top-gated structure. At this point, it is worthwhile to remark that gating has been an essential tool to unveil the exotic and unprecedented phenomena in graphene. With gating, it is possible to tune the Fermi energy as well as to create potential barriers in graphene.[21,22] The Dirac-fermion quantum motion is biased into the Q1D nanoribbon (along the x direction) by two top voltage gates represented with plates A and B (blue), whereas the third top voltage gate, shown as plate V_b (blue), creates an arbitrary square-potential quantum barrier (QB) located at almost a quarter of the quantum-channel right border (see Fig. 3). Within the under-QB space, the locally-induced SOI-R coupling is electrostatically tuned. This way we are able to explore pseudospin-related effects, and the dynamics of Dirac fermions betoken as a one-dimensional Gaussian wave packet (1DGWP) drift in the free-space region, as well as inside the scatterer, with a group velocity of two orders less than light speed.[15] Figure 3 depicts an instance of this phenomenology.
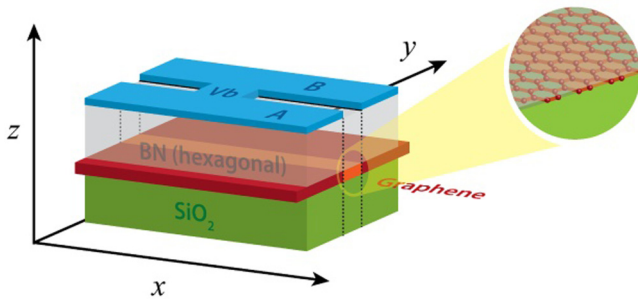

FIG. 2. Diagrammatic representation of the setup displaying a 3D-perspective view of the proposed spintronic device. Two-dimensional monolayer graphene surface (red), with a lithographically printed narrow nanoribbon (middle yellow strip) sandwiched by a film of hexagonal boron nitride (hBN, transparent gray) and a silicon dioxide (SiO₂, green) substrate. The Dirac-fermion quantum motion is biased into the quasi-one-dimensional nanoribbon (along the x direction) by top voltage gates represented with plates A and B (blue). Whereas the third top voltage gate, shown as plate V_b (blue), creates the quantum potential barrier, under which the locally-induced SOI-R coupling is manipulated.
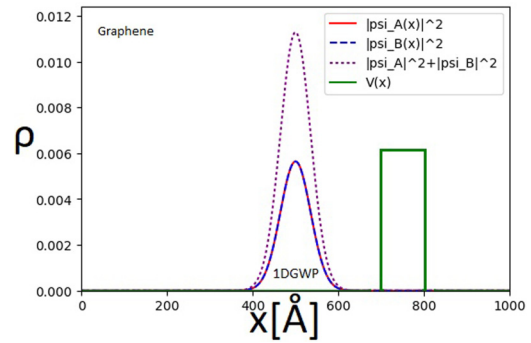

FIG. 3. Physical system in its initial state $t = 0$ fs, where the green solid line represents a potential barrier [with $V(x) \neq 0$ eV only in the interval $x \in [700, 800]$ Å and $V(x) = 0$ eV elsewhere]. The solid red line is the probability density of the A component of (3), the dashed blue line is for the B component of (3), while the dotted purple one is the sum of both components of the pseudospinor.

III. THEORETICAL AND MATHEMATICAL OUTLINES

A. Pristine graphene

We have assumed free massless Dirac fermions at low energies. Then, near the $K(K')$ points, the pristine MLG Dirac-like Hamiltonian becomes

$$\hat{H}_0 = v_F \vec{\boldsymbol{\sigma}} \cdot \vec{p}, \tag{1}$$

with $\vec{\boldsymbol{\sigma}} = \hat{\boldsymbol{\sigma}}_x \hat{i} + \hat{\boldsymbol{\sigma}}_y \hat{j}$ being the pseudospin Pauli matrices $\hat{\boldsymbol{\sigma}}_x = \begin{pmatrix} 0 & 1 \\ 1 & 0 \end{pmatrix}$, $\hat{\sigma}_y = \begin{pmatrix} 0 & -i \\ i & 0 \end{pmatrix}$, and $\vec{p} = \hat{p}_x \hat{i} + \hat{p}_y \hat{j}$, the momentum operator, whose x, y components read $\hat{p}_x = -i\hbar \frac{\partial}{\partial x}$ and $\hat{p}_y = -i\hbar \frac{\partial}{\partial y}$, respectively. Hereinafter, v_F stands for the Fermi velocity of the carriers in MLG, which satisfies

$$v_F \approx \frac{c}{300}. \tag{2}$$

In particular, this means that, on general grounds, for the QED specific phenomena of our interest (PZBE, Klein, and anti-Klein tunneling), the pseudospin-related effects should prevail those with a real spin dependency.[3] Finally, the dispersion law has the widely-known form $E = \pm |\hbar k| v_F$, where $\pm$ refers to the electron (hole) band. Another striking characteristic of the MLG is the well-known chirality or helicity. Indeed, the momentum operator for the Dirac fermions in sublattice A has a preferential settling of its projection along the pseudospin direction, while for the Dirac fermions in sublattice B, it is found completely opposite. For this reason, the pseudospinor is a two-component state of the form,

$$\boldsymbol{\Psi}(x, t) = \begin{pmatrix} \psi_A(x, t) \\ \psi_B(x, t) \end{pmatrix}. \tag{3}$$

B. Rashba spin–orbit interaction

Very precise atomic-resolution scanning-tunneling microscopy images revealed, for the first time, the presence of a strong spatially-dependent perturbation, which breaks the hexagonal lattice symmetry of a 2D MLG, supported by a SiO_2 substrate.[17] This experimental evidence has shown that the strain-induced corrugations break the 2D honeycomb lattice configuration of the 2D MLG and thus may explicitly produce a short-range localized structural inversion asymmetry (SIA), causing the extrinsic SOI-R to arise. Besides, an accidental doping in the SiO_2 substrate (due to, for example, the presence of atmospheric species) may also provoke lattice asymmetries, which yield SOI-R via Stark interaction with the impurities.[15] Even by optimizing the SiO_2 substrate upon which the 2D MLG is deposited to conform the test device (see Fig. 2), the Rashba term can be dominant.[23] Another viable scenario for a locally-induced SOI-R is to add light adatoms such as hydrogen. This atmospheric component, even within the dilute limit, is a good precursor of enhanced SOI-R effects in graphene, which as an added bonus do not sensibly modify the zero gap Dirac cones spectrum.[2] The authors of the quantitative measures demonstrating locally-spaced extrinsic-induced SIA[17] share the opinion that these kinds of experimental support can be used as inputs to theoretical models to study the effects of SOI-R on quantum transport properties.[17] In short, if space inversion symmetry of graphene is broken by the substrate, external electric fields, or adatoms, the SOI-R appears.[2]

On the other hand, the SOI-R in graphene was also considered reachable with standard gating.[15] So, in principle, the top-gated device proposed in Fig. 2 could perfectly induce SOI-R. Once we adopt gating, the fact is that graphene is no longer pristine and the Hamiltonian (1) needs to be complemented with two contributions, namely, intrinsic SOC and extrinsic SOI.[15,23–25] There is another significant issue to be considered, which is the band-structure topology of graphene with SOC. Touching Dirac cones exist only for pristine graphene whenever the SOC is neglected. As long as it is present, the orbital degeneracy at the Dirac points is lifted and the SOC gap appears.[26] It is interesting to observe SOI effects in a Q1D MLG nanoribbon of the device shown in Fig. 2, but without destroying the structure of pristine graphene Dirac cones much. It is then necessary to fix the external electric field to certain values, at which the intrinsic and extrinsic Bychkov–Rashba SOC parameters are equal ($\lambda_I = \lambda_R$, respectively). Then, two bands with the same pseudospin index form touching Dirac cones again, still preserving the linear dispersion law;[2,26] meanwhile, the other two remain apart. In fact, it is more convenient to assume the case when $\lambda_R > \lambda_I$, which allows us to neglect the intrinsic SOC. So, the combined Hamiltonian can be written as[26]

$$\hat{H}_{MLG} = \hat{H}_0 + \hat{H}_{BR} = v_F(\eta\hat{\sigma}_x p_x + \hat{\sigma}_y p_y) + \lambda_R(\eta\hat{\sigma}_x \mathbf{S}_y - \hat{\sigma}_y \mathbf{S}_x), \quad (4)$$

where the second term represents the extrinsic SOC of Bychkov–Rashba,[26] $\mathbf{S}_{x,y}$ stands for the real spin Pauli matrices, and $\eta = \pm 1$ is taken for the cones at $K(K')$, respectively. Equation (4) has been commonly applied for 2D MLG or graphene-based 2D systems.[26,27] In our case, we are considering a Q1D system as the one given in Fig. 2, and no Hamiltonian has been reported yet that accounts for the SOI-R for a Q1D MLG nanoribbon, as far as we know.

By considering the striking experimental detection of heavy holes (hh), with an effective mass of $m_{hh} \approx 0.1m_o$ via Shubnikov–de Haas oscillations in a system of FLG,[21] we are assuming that the momentum-dependent term of the well-known Rashba Hamiltonian for Q1D semiconductor heterostructures[28,29] can be extended to the context of Q1D graphene structures. To what extent this assumption is correct will depend on a formal derivation of the corresponding Hamiltonian under the geometrical and structural conditions of our system and/or experimental results that support or dismiss it. The uncommon properties of the 2D FLG,[21] supported on nonzero mass carriers, are not expected to manifest themselves and have yet to be understood. Moreover, on such grounds it is cumbersome to clarify to date if a formally derived Q1D Hamiltonian for an MLG (so far, we are not aware of any) will be equivalent for both electrons and holes in a single shoot. Taking into account all these considerations, together with the fact that to travel into the under-QB region, Dirac fermions tunnel as free holes[30] (sometimes by means of Klein tunneling), we substitute $\hat{H}_{BR}$ in (4). First, we make a departure from a Rashba Hamiltonian for holes[28]

$$\hat{H}_{SOI-R} = -i\alpha\left[\frac{\hat{k}_-^2}{\hat{k}_+}\sigma_+ - \frac{\hat{k}_+^2}{\hat{k}_-}\sigma_-\right] - i\beta\left[\hat{k}_-^3\sigma_+ - \hat{k}_+^3\sigma_-\right], \quad (5)$$

where $\hat{k}_\pm = (\hat{k}_x \pm i\hat{k}_y)$, $\sigma_\pm = \frac{1}{2}(\sigma_x \pm i\sigma_y)$, α is the linear Rashba parameter, and β is the cubic Rashba parameter (both of them are material-dependent constants). Finally, after some algebra, and by zeroing the components accompanying $\hat{k}_y$, we obtain an effective Q1D Hamiltonian for the hole branch[29]

$$\hat{H}_{SOI-R} = (-i\alpha\partial_x + i\beta\partial_x^3)\sigma_y, \quad (6)$$

where $\partial_x = \frac{\partial}{\partial x}$. Thus, expression (6) is used instead of $\hat{H}_{BR}$ in (4) to obtain partial answers to the question related to the main purpose of the present study (see Sec. I), a question that will be addressed soon.

C. Hybrid Hamiltonian: Finite differences scheme

The hybrid Hamiltonian to deal with for achieving the envisioned goals outlined in Sec. I, for the physical-system device depicted in Fig. 2, will be the summation of the pristine MLG Dirac-like Hamiltonian (1), with the components $\hat{k}_y = 0$, the SOI-R Hamiltonian (6), and the potential $V(x)$ representing our QB created by gating.[30] This leads to the crucial equation

$$\hat{H} = \hat{H}_0 + \hat{H}_{SOI-R} + V(x)\mathbb{I}_2$$
$$= \begin{pmatrix} V(x) & -i\hbar v_f\partial_x - \alpha\partial_x + \beta\partial_x^3 \\ -i\hbar v_f\partial_x + \alpha\partial_x - \beta\partial_x^3 & V(x) \end{pmatrix}, \quad (7)$$

where $\mathbb{I}_2$ stands for the second order identity matrix. Let us consider a square QB (see Fig. 3, green solid line), in the interval $x \in [700, 800]$ Å of thickness $\Delta x_b = 100$ Å and given by $V(x) = V_0\mathcal{H}(x)$, with $\mathcal{H}(x)$ being the Heaviside step function. We impose $\mathcal{H}(x) = 1; \forall x \in [700, 800]$ Å and $\mathcal{H}(x) = 0$, otherwise. For the time being, we consider that the hybrid Hamiltonian (7)

captures the essential physics of our envisioned problem, as we shall demonstrate in Sec. IV. We proceed further by discussing the time-dependent Dirac-like equation in a Q1D space, though writing it as an evolution equation within the standardized Schrödinger frame. The time evolution in the free (scattering)-space region, resulting from the diffusion under arbitrary initial conditions, can be an excellent workbench for the finite difference scheme. So, for the mathematical procedure, we turn the Q1D Dirac-like equation (7), within the framework of the familiar Schrödinger model, into a discrete formulation

$$(\hat{H}\Psi(x,t))_j^n = \imath\hbar \frac{\partial}{\partial t}\Psi(x,t)_j^n, \tag{8}$$

where n is the discretization variable of time, while j is the discretization variable of space, so that $t \to n\delta t$ and $x \to j\delta x$; for $n = 1, 2, \ldots, N$ and $j = 1, 2, \ldots, J$, respectively. The elemental quantity $\delta x(\delta t)$ quotes the space(time) minimal step of the grid. The general solution for (8) can be proposed in the form,

$$\Psi(x,t) = \hat{U}(t,t_0)\Psi(x,t_0), \tag{9}$$

where $\hat{U}(t,t_0)$ is the time-evolution operator, which is defined as

$$\hat{U}(t,t_0) = e^{\frac{\imath}{\hbar}\delta t \hat{H}}. \tag{10}$$

First, it is convenient to use Cayley's approach,[28]

$$\hat{U}(t,t_0) = \frac{2\mathbb{I}_2}{\mathbb{I}_2 + \frac{1}{2}\frac{\imath\delta t}{\hbar}\hat{H}} - \mathbb{I}_2, \tag{11}$$

and by substituting (11) in (9), we obtain

$$\Psi(x,t) = \Phi(x,t_0) - \Psi(x,t_0), \tag{12}$$

where

$$\Phi(x,t_0) = \frac{2\Psi(x,t_0)}{\mathbb{I}_2 + \frac{1}{2}\frac{\imath\delta t}{\hbar}\hat{H}}. \tag{13}$$

It is clear from (13) that

$$2\Psi(x,t_0) = \Phi(x,t_0) + \frac{\imath\delta t}{2\hbar}\hat{H}\Phi(x,t_0), \tag{14}$$

which is solved for $\Phi(x,t_0)$, to be further substituted in (12), whose discrete form can be cast as

$$\Psi_j^{n+1} = \Phi_j^n - \Psi_j^n. \tag{15}$$

Now, we impose the initial boundary conditions,

$$\Psi_{j=0}^{n=0} = \Psi_{j=J}^{n=0} = 0, \tag{16}$$

to calculate the wave functions along the Q1D nanoribbon, sketched in Fig. 2 (yellow strip). The standard Taylor development is performed for functions evaluated in $j-2$; $j-1$; $j+1$, and $j+2$. Afterward, we solve the equation system for the derivatives and we get

$$\psi_j' = \frac{\psi_{j-2} - 8\psi_{j-1} + 8\psi_{j+1} - \psi_{j+2}}{12\delta x}, \tag{17}$$

$$\psi_j'' = \frac{-\psi_{j-2} + 16\psi_{j-1} - 30\psi_j + 16\psi_{j+1} - \psi_{j+2}}{12\delta x^2}, \tag{18}$$

$$\psi_j''' = \frac{-\psi_{j-2} + 2\psi_{j-1} - 2\psi_{j+1} + \psi_{j+2}}{2\delta x^3}, \tag{19}$$

$$\psi_j'''' = \frac{\psi_{j-2} - 4\psi_{j-1} + 6\psi_j - 4\psi_{j+1} + \psi_{j+2}}{\delta x^4}. \tag{20}$$

By substituting (7) in (14), using (17)–(20), after adding and subtracting both components of (14), we finally reach the crucial equation systems,

$$2(\psi_{Aj} + \psi_{Bj}) = MA_b P_{j-2} - 8MA_b P_{j-1} + (1+MV)P_j + 8MA_b P_{j+1} - MA_b P_{j+2} + MB_a Q_{j-2} - MC_a Q_{j-1} + MC_a Q_{j+1} - MB_a Q_{j+2}, \tag{21}$$

$$2(\psi_{Aj} - \psi_{Bj}) = -MB_a P_{j-2} + MC_a P_{j-1} - MC_a P_{j+1} + MB_a P_{j+2} - MA_b Q_{j-2} + 8MA_b Q_{j-1} + (1+MV)Q_j - 8MA_b Q_{j+1} + MA_b Q_{j+2}, \tag{22}$$

where $M = (\imath\delta t)/(2\hbar)$, $A_b = (A_a)/(12\delta x)$, $A_a = -\imath\hbar v_f$, $B_a = (\alpha\delta^2 x + 6\beta)/(12\delta^3 x)$, and $C_a = (2\alpha\delta^2 x + 3\beta)/(3\delta^3 x)$. The quantities we are looking for are P_j and Q_j, since

$$\phi_{(A,B)j} = \frac{1}{2}\left[P_j \pm Q_j\right]. \tag{23}$$

Considering that we have P_j and Q_j in both equation systems (21) and (22), they can be treated as $(J \times 1)$ vectors, as well as the terms $2(\psi_{Aj} + \psi_{Bj})$ and $2(\psi_{Aj} - \psi_{Bj})$. Besides, for convenience, the physical system's constants will be embedded in the $(J \times J)$ matrices $\mathbb{M}_{A,B}$, which are 5-diagonal ones of the form

$$\mathbb{M}_A = \begin{pmatrix} (1+MV) & 8MA_b & -MA_b & 0 & 0 & \dots & 0 \\ -8MA_b & (1+MV) & 8MA_b & -MA_b & 0 & \dots & 0 \\ MA_b & -8MA_b & (1+MV) & 8MA_b & -MA_b & \dots & 0 \\ 0 & \ddots & \ddots & \ddots & \ddots & \ddots & 0 \\ \vdots & \vdots & \vdots & \vdots & \vdots & \vdots & \vdots \\ 0 & \dots & MA_b & -8MA_b & (1+MV) & 8MA_b & -MA_b \\ 0 & \dots & 0 & MA_b & -8MA_b & (1+MV) & 8MA_b \\ 0 & \dots & 0 & 0 & MA_b & -8MA_b & (1+MV) \end{pmatrix} \quad (24)$$

and

$$\mathbb{M}_B = \begin{pmatrix} 0 & MC_a & -MB_a & 0 & 0 & \dots & 0 \\ -MC_a & 0 & MC_a & -MB_a & 0 & \dots & 0 \\ MB_a & -MC_a & 0 & MC_a & -MB_a & \dots & 0 \\ 0 & \ddots & \ddots & \ddots & \ddots & \ddots & 0 \\ \vdots & \vdots & \vdots & \vdots & \vdots & \vdots & \vdots \\ 0 & \dots & MB_a & -MC_a & 0 & MC_a & -MB_a \\ 0 & \dots & 0 & MB_a & -MC_a & 0 & MC_a \\ 0 & \dots & 0 & 0 & MB_a & -MC_a & 0 \end{pmatrix}. \quad (25)$$

Thus, we define

$$\mathbf{\Psi}_+ = \mathbb{M}_A \cdot \mathbf{P} + \mathbb{M}_B \cdot \mathbf{Q}, \quad (26)$$

$$\mathbf{\Psi}_- = \mathbb{M}_B^T \cdot \mathbf{P} + \mathbb{M}_A^T \cdot \mathbf{Q}, \quad (27)$$

and after a not too hard algebra, we can obtain

$$\mathbf{Q} = \left[\mathbb{M}_A^T - \mathbb{M}_B^T \cdot \left(\mathbb{M}_A^{-1} \cdot \mathbb{M}_B\right)\right]^{-1} \cdot \left[\mathbf{\Psi}_- - \mathbb{M}_B^T \cdot \left(\mathbb{M}_A^{-1} \cdot \mathbf{\Psi}_+\right)\right], \quad (28)$$

$$\mathbf{P} = \mathbb{M}_A^{-1} \cdot (\mathbf{\Psi}_+ - \mathbb{M}_B \cdot \mathbf{Q}). \quad (29)$$

In short, to simulate the time evolution, resulting from the quantum diffusion (scattering) of Dirac fermions, whenever they move in the free(QB) regions of a Q1D MLG nanoribbon of the device shown in Fig. 2, we first solve (28) and (29) for P_j and Q_j, respectively, next we find ϕ_{Aj} and ϕ_{Bj} from (23), to substitute afterward in (15). The latter procedure is a cyclic $(n = 1, \dots, N)$-time loop for each of the $(j = 1, \dots, J)$-space points.

IV. DISCUSSION OF RESULTS

Let us start exposing the use of the hybrid Hamiltonian (7), within the finite difference scheme developed in Sec. III C, for the examination of several pseudospin-related effects during the quantum transport of a 1DGWP along a Q1D MLG narrow nanoribbon embedded into the spintronic device shown in Fig. 2. Wherever possible, a comparison with available experimental or numerical results will be made. We have gathered worldline pictures of the envisioned Dirac-fermion quantum diffusion (scattering) for several physical conditions of interest, and the correspondent multimedia are available to be consulted and/or downloaded from a permanent weblink (see Ref. 31). For the timeline animations, we used a box of length $L = 500\,\text{Å}$ (see the abscissa axis of Fig. 3) and a simulation time of 50 fs. The centroid of the Gaussian wave packet was allocated at $x_0 = 250\,\text{Å}$, while the dispersion size was fixed as $\sigma = 50\,\text{Å}$, and a barrier thickness of $\Delta x_b = 100\,\text{Å}$ was taken. It is important to mention that, for the quantum diffusion (scattering) to be stable, we must follow the requirement

$$\delta t \leq \frac{\delta x^2}{2}, \quad (30)$$

which as an added bonus becomes unexpectedly relevant to our study, provided we have demonstrated its influence to resolve several fine features of the wave-packet diffusion to compare with.[8] For describing the dynamics of the Dirac fermions in an MLG-based Q1D nanoribbon (see Fig. 2), we have represented them by a 1DGWP defined as

$$\mathbf{\Psi}(x, t=0) = \frac{\xi}{\sigma}\sqrt{\frac{1}{\pi}}\,e^{-\frac{(x-x_0)^2}{2\sigma^2}}\,e^{ik(x-x_0)}, \quad (31)$$

whose group velocity decreases proportionally to δt, remaining shorter than light speed. The following set of the real-spin shape

$$\xi = \begin{pmatrix} 1 \\ 0 \end{pmatrix}, \quad \xi = \frac{1}{\sqrt{2}}\begin{pmatrix} 1 \\ 1 \end{pmatrix}, \quad \xi = \frac{1}{\sqrt{2}}\begin{pmatrix} 1 \\ i \end{pmatrix}, \quad \text{and} \quad \xi = \frac{1}{\sqrt{2}}\begin{pmatrix} 1 \\ e^{i\pi/4} \end{pmatrix}$$

unambiguously determines the four different cases of the initial pseudospinor configuration (PSC) we are interested in, for comparison with a prior study,[8] pursuing a validation of our model.

In this section, we divide the discussion into three parts. First, there is a semiquantitative comparison for a Dirac-fermion 1DGWP in the free space between our results and those published elsewhere.[8] Second, we analyze the dynamics of the 1DGWP during its drift, when sampling in the vicinity of the Dirac points K and K' (see Fig. 1), as well as far from them. Finally, we try to study whether the under-barrier biased SOI-R interplays during the Dirac-fermion interaction with the QB. We underline the usefulness of expression (30) (directly derived from our model) to stabilize the quantum diffusion (scattering) in the free-space (under-barrier) regions, respectively, and to resolve several fine features of the wave-packet diffusion to compare with.[8] Readers could verify the remarkably good qualitative agreement of all Fig. 4 panels, with those of Ref. 8, for the same initial pseudospin configurations. Notice that we were able to accurately reproduce even the small shoulders.

In Fig. 4, we show the timeline evolution of the 1DGWP in the free-space region $[V(x) = 0, \alpha \equiv \beta = 0]$, resulting from the quantum diffusion of Dirac fermions modeled by the 1DGWP (31), along the Q1D MLG narrow nanoribbon of the proposed device (see Fig. 2). We have assumed a width less than the lattice parameter. As can be seen, the 1DGWP spreads and ultimately divides into a couple of variable-shape sub-1DGWPs, which drift apart with respect to the center of the box, as expected.[8] In all panels, the probability density of each pseudospinor component $\rho_{A,B} = |\psi_{A,B}|^2$ is represented with a red-solid (blue-dashed) line. Meanwhile, the conservation law $\rho = |\psi_A|^2 + |\psi_B|^2$ is depicted with a purple-dotted line. Next, a case-by-case comparison between our data with several graphs obtained by Frolova et al.[8] for an identical PSC set is presented and a good qualitative agreement is achieved. For the sake of accuracy, we first "cut" their 3D wave packet (WP) along their x/d axis at $y/d = 0$ (see Fig. 1 in Ref. 8). Thereby, panels (a)–(d) show a projection of the 1DGWP (31) worldline on that cut plane. In panel (a), with $\xi = \begin{pmatrix} 1 \\ 0 \end{pmatrix}$, the 1DGWP (31) turns divided into two smaller sub-1DGWPs with the same amplitude that begin moving in opposite directions (see Fig. 1 in Ref. 8). In panel (b), when $\xi = \frac{1}{\sqrt{2}}\begin{pmatrix} 1 \\ 1 \end{pmatrix}$, the 1DGWP becomes divided differently, but it continues to move in the positive direction of x (see Fig. 3 in Ref. 8). Panel (c) plots the evolution for the PSC $\xi = \frac{1}{\sqrt{2}}\begin{pmatrix} 1 \\ i \end{pmatrix}$ and the split sub-1DGWP is similar in the amplitude of $|\psi_{A,B}|^2$, though slightly less than that of panel (a) (see Fig. 5 in Ref. 8). Finally, panel (d) displays the case for PSC $\xi = \frac{1}{\sqrt{2}}\begin{pmatrix} 1 \\ e^{i\pi/4} \end{pmatrix}$, and the WP is divided into two sub-1DGWPs; however, the one on the left is smaller compared to the one on the right (see Fig. 7 in Ref. 8). It is worthwhile to stress that inner-side small ripples were detected solely under the fulfillment of (30), by fixing a time partition of $c\delta t$ with $c \in [0.5, 1]$. The most important point to note here is that when the 1DGWP is
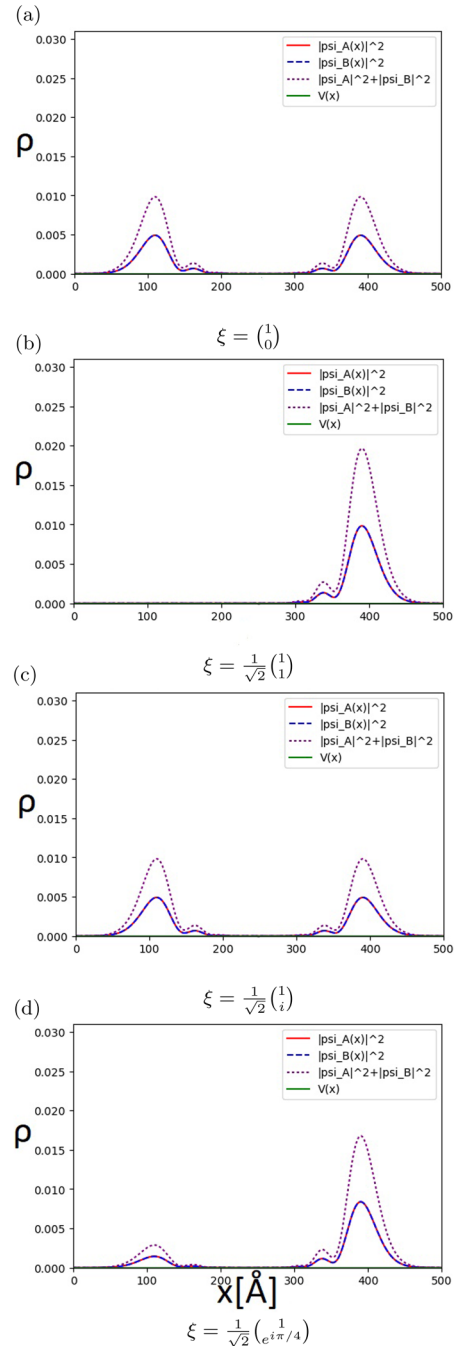

FIG. 4. Worldline dynamical drift of our 1DWGP in the free-space region $[V(x) = 0, \alpha \equiv \beta = 0]$ at $t = 20$ fs and given values of ξ, for a qualitative comparison with the wave packet at a similar time interval and with the same ξ configurations as in Ref. 8. On panels (a) and (c), the 1DGWP spreads and ultimately divides into a couple of identical sub-1DGWPs with two local maxima. Panel (b) shows a drifting 1DGWP, whose height is bigger compared with (a), due to the conservation of probability density. Finally, panel (d) presents split sub-1DGWPs as in panel (a), but this time, the one at the right has the biggest ρ.

located at point K of the reciprocal lattice ($k_{x,y} = 0$) (see Fig. 1), no oscillations of $|\psi_{A,B}|^2$ were detected. Multimedia of the Dirac-fermion worldline dynamic in the free space are available in a permanent weblink (see Ref. 31).

Figure 5 plots the foremost contribution of the present study, i.e., the stable evidence of antiphase oscillations in the probability density time-distribution for each pseudospinor component $|\psi_{A,B}|^2$ of the corresponding sublattice state (3), when the 1DGWP travels along the Q1D device of Fig. 2 in the free-space region. These oscillations resemble those of the wiggling motion discovered by Schrödinger,[6] but in this case for $\rho_{A,B} = |\psi_{A,B}|^2$. Thus, we have named the phenomenology described here as pseudospinorial *Zitterbewegung* effect [see panels (e), (g), and (h)]. In all panels, we have represented $|\psi_A|^2$ with a red-solid line and $|\psi_B|^2$ with a blue-dashed one. For the selected parameters' rank, the conservation requirement $\rho = |\psi_A|^2 + |\psi_B|^2$ was carefully verified and displayed by a purple-dotted line everywhere. First, the 1DGWP was allocated at the Dirac point K (see Fig. 1), afterward it was released to drift along the 500 Å L-length box described above. No oscillations of $|\psi_{A,B}|^2$ were detected at all, but despite this, we explored several PSCs [see left-column panels (a)–(d)]. Interestingly, by now replacing the 1DGWP center mass away from K, clear $|\psi_{A,B}|^2$ oscillations were detected when it drifts in the box, whose shape strongly depends on the initial PSC, as can be clearly seen from right-column panels (e), (g), and (h). Indeed, for $\xi = \begin{pmatrix} 1 \\ 0 \end{pmatrix}$ [see panel (e)], $|\psi_{A,B}|^2$ maximizes (minimizes) at $t = 0$, meanwhile they start from the same amplitude for $\xi = \frac{1}{\sqrt{2}} \begin{pmatrix} 1 \\ \imath \end{pmatrix}$ [see panel (g)]. Panel (h) shows a similar feature to the latter one, though with a reduced amplitude of $|\psi_{A,B}|^2$ for $\xi = \frac{1}{\sqrt{2}} \begin{pmatrix} 1 \\ e^{\imath\pi/4} \end{pmatrix}$. Having accomplished a semiempirical method (32)—to be detailed described below—and taking all the values of Table I into account, the simulation results of right-column panels (e)–(h) were confirmed and accurately described by this methodology. Since the constants D and E do not nullify simultaneously for all PSCs (see Table I), the sinusoidal-dependent function Us(t) in (32) survives, yielding the PZBE oscillations to rise [see right-column panels (e), (g), and (h)]. During numerical explorations, unexpectedly for a fully symmetric PSC $\xi = \frac{1}{\sqrt{2}} \begin{pmatrix} 1 \\ 1 \end{pmatrix}$ [even at $k_{x(y)} = 0.09(0)$ Å^{-1}], the PZBE vanishes [see panel (f)]. Again, after the computation with (32), this is not surprising given the fact that a simultaneous zeroing of the parameters D and E for $\xi = \frac{1}{\sqrt{2}} \begin{pmatrix} 1 \\ 1 \end{pmatrix}$ (see Table I) leads the periodic function in (32) to nullify, and thereby no oscillations can be expected at that PSC. Good qualitative agreement with previous reports of the ZBE in graphene[1,8,13,14] has been achieved, because a robust transient character of the oscillations, with a decay time of about 10.5 fs, was found in all cases under examination here. Multimedia for the trembling dynamics of Dirac fermions in the free space are available in a permanent weblink (see Ref. 31), and thus the rise of the PZBE via $|\psi_{A,B}|^2$ antiphase oscillations can be more explicitly observed in colored worldline pictures.
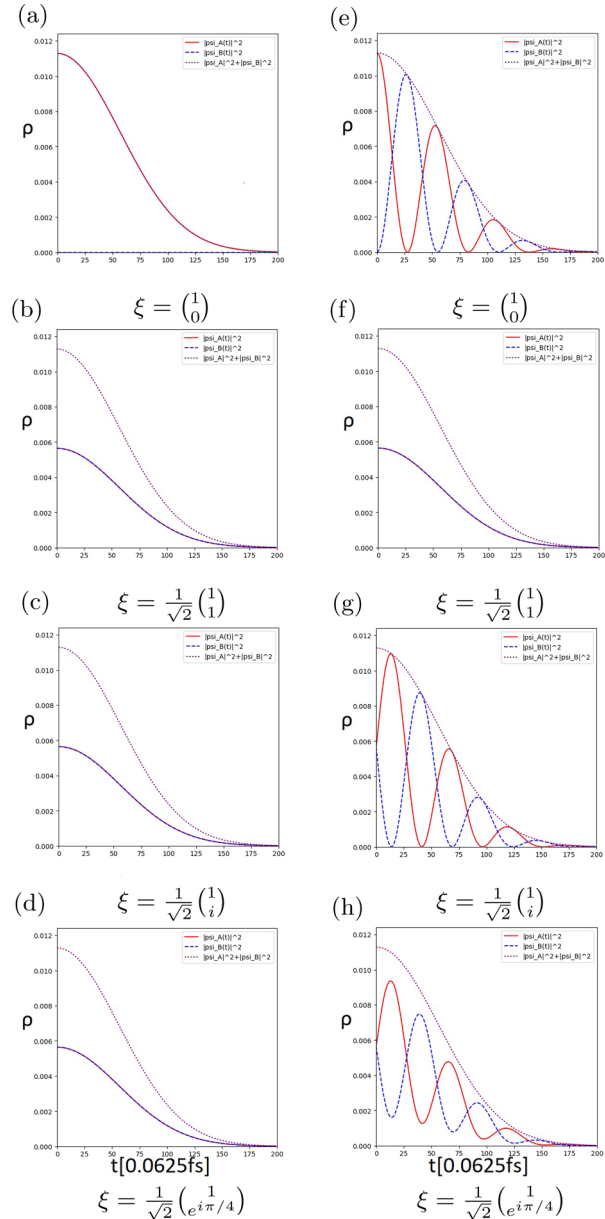

FIG. 5. Qualitative comparison for probability density $|\psi_{A,B}|^2$ as a function of time, at $k_{x,y} = 0$ (left-column panels), with that of $k_{x(y)} = 0.09(0)$ Å^{-1} (right-column panels), for the free-space case. Panel (a) shows finite $\rho_A = |\psi_A|^2$ values solely, because $\rho_B = |\psi_B|^2$ zeroed. Panels (b)–(f) display an identical evolution of $\rho_{A,B}$, despite the different ξ, though starting with the same probability-density amplitude. Importantly, panels (e), (g), and (h) show the antiphase oscillations of $\rho_{A,B}$, named after PZBE.

Figure 6 is devoted to demonstrate the dependence of PZBE frequency on $k_{x(y)}$ during the passage of the 1DGWP in the free space. Notice the difference in comparison with the right-column panels: (e), (g), and (h) of Fig. 5, i.e., the higher the $k_{x(y)}$ values, the

TABLE I. Numerical estimation for coefficients of (32) for several initial PSCs at $k_{x(y)} = 0.09(0)\,\text{Å}^{-1}$. RMSU stands for the root mean square uncertainty.

Constant	$\xi = \begin{pmatrix} 1 \\ 0 \end{pmatrix}$	$\xi = \frac{1}{\sqrt{2}}\begin{pmatrix} 1 \\ 1 \end{pmatrix}$	$\xi = \frac{1}{\sqrt{2}}\begin{pmatrix} 1 \\ i \end{pmatrix}$	$\xi = \frac{1}{\sqrt{2}}\begin{pmatrix} 1 \\ e^{i\pi/4} \end{pmatrix}$
C	0.00	0.00	0.00	0.71
$D(\text{fs}^{-1})$	20.00	0.00	20.00	20.00
E	$\pi/2$	0.00	0.00	0.00
$F(\text{fs}^{-2})$	-0.04	-0.04	-0.04	-0.04
RMSU	6.27×10^{-6}	1.24×10^{-7}	1.91×10^{-6}	2.20×10^{-5}

smaller the $|\psi_{A,B}|^2$ oscillation period. For instance, by letting grow k_x in about one order, the period diminishes almost to a half [see Fig. 5(h) for the purposes of comparison]. We realize that effects such as this k-dependence in the PZBE play an important role in the modifications of its oscillation period. There is no any straightforward derivation of this behavior from the theoretical model presented above (see Sec. III). It was then necessary to obtain an explicit analytic equation to fit the observed k-dependent oscillating patterns of the PZBE. Performing a semiempirical numerical method on testing grounds, we obtained a function of the time that describes quite accurately the oscillating behavior for each $\rho_{A,B} = |\psi_{A,B}|^2$ component and can be expressed as follows:

$$\rho_{s\xi}(500, t) = U_s(t)\rho_{s\xi}(500, 0), \qquad (32)$$

where $U_s(t) = \frac{1}{2}[\pm C \sin(Dt + E) + 1]\,e^{Ft^2}$, for $s = A, B$, respectively. It is worthwhile stressing that procedure (32), although not an explicit function of k, is well chosen and reliably reproduces the k-dependent PZBE oscillating features of Fig. 6 (see red-solid and blue-dashed lines for each sublattice component). The logic behind $U_s(t)$ can be interpreted as a comprehensive analog with the time-evolution-operator solution in (9), but for the probability density. In that sense, (32) emerges as a valid model for describing the dynamic properties of the envisioned 1DGWP. By summing up both expressions of $U_s(t)$ in (32), we get

$$\rho_\xi(500, t) = e^{Ft^2}\rho_\xi(500, 0), \qquad (33)$$

which is a practical and simplified expression for the envelope probability density $\rho = |\psi_A|^2 + |\psi_B|^2$ (see the purple-dotted line of Figs. 5 and 6), though preserving the time-evolution analogy commented above.

If one releases the 1DGWP in the vicinity of the Γ point (see Fig. 1), the group velocity diminishes and tends rapidly to zero by approaching it. In other words, the 1DGWP becomes almost static; while the frequency of PZBE oscillations is so high that it would seem at first sight that there are no oscillations at all (see animations of Ref. 31). We numerically verified that the parameters D and F are the ones that behave as certain functions of k_x. Indeed, D is directly proportional to k_x, while F shows an inverse proportionality to it. Both of them clearly define the periodic and the envelope parts, respectively, of time-evolution operatorlike functions (32) and (33). Thus, the frequency increment when k_x grows (by approaching the Γ point), together with the robust decay of about 10.5 fs, is very likely because, first, D having units

of (fs^{-1}) belongs to the harmonic function in (32); and second, the exponential part of (33) depends on F, which is in addition, a negatively defined quantity (see Table I). Undoubtedly, a much deeper theoretical analysis is achievable as well as required on this relevant PZBE k-dependence. However, we do not believe it would significantly modify our results, and in all likelihood, it would just follow the trends we show here, albeit some refinement could be expected specially in the vicinity of the high-symmetry points of reciprocal space.

To this end, the main findings discussed from Figs. 5 and 6 are highlighted, i.e., the undoubted evidence of the PZBE during the passage of Dirac fermions along a Q1D channel, formed by a narrow nanoribbon sandwiched in a novel top-gated structure (see Fig. 2), and the k-dependent tunable behavior of the PZBE. Both of them are strictly independent of the terms $V(x)$ and $\hat{H}_{\text{SOI-R}}$ in (7) because they have been nullified, reinforcing, in this way, the essential link of these events to the pristine MLG Hamiltonian $\hat{H}_0$ (1) presented in Sec. III A.

Finally, let us turn to the third part of this section, in which we will try to provide evidence on whether or not the under-barrier biased SOI-R according to (7) influences the Dirac fermions during their tunneling throughout the QB.

Figure 7 displays what happens with the 1DGWP after $t = 12.5$ fs, considering the interaction with a QB under SOI-R. We can observe for $k_x \approx 0$ and $k_y = 0$ (left-column panels) that Dirac
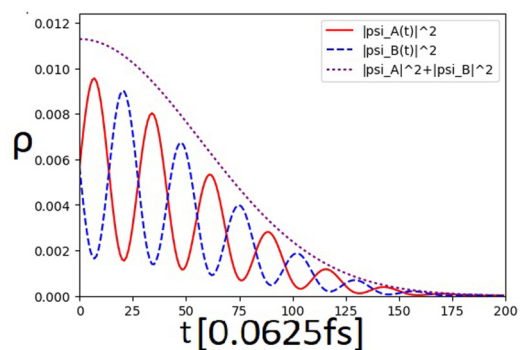

FIG. 6. PZBE through the evolution of the probability density $|\psi_{A,B}|^2$ as a function of time during the first 12.5 fs of the 1DGWP drift in the free space, at $k_{x(y)} = 0.18(0)\,\text{Å}^{-1}$ and $\xi = \frac{1}{\sqrt{2}}\begin{pmatrix} 1 \\ e^{i\pi/4} \end{pmatrix}$.
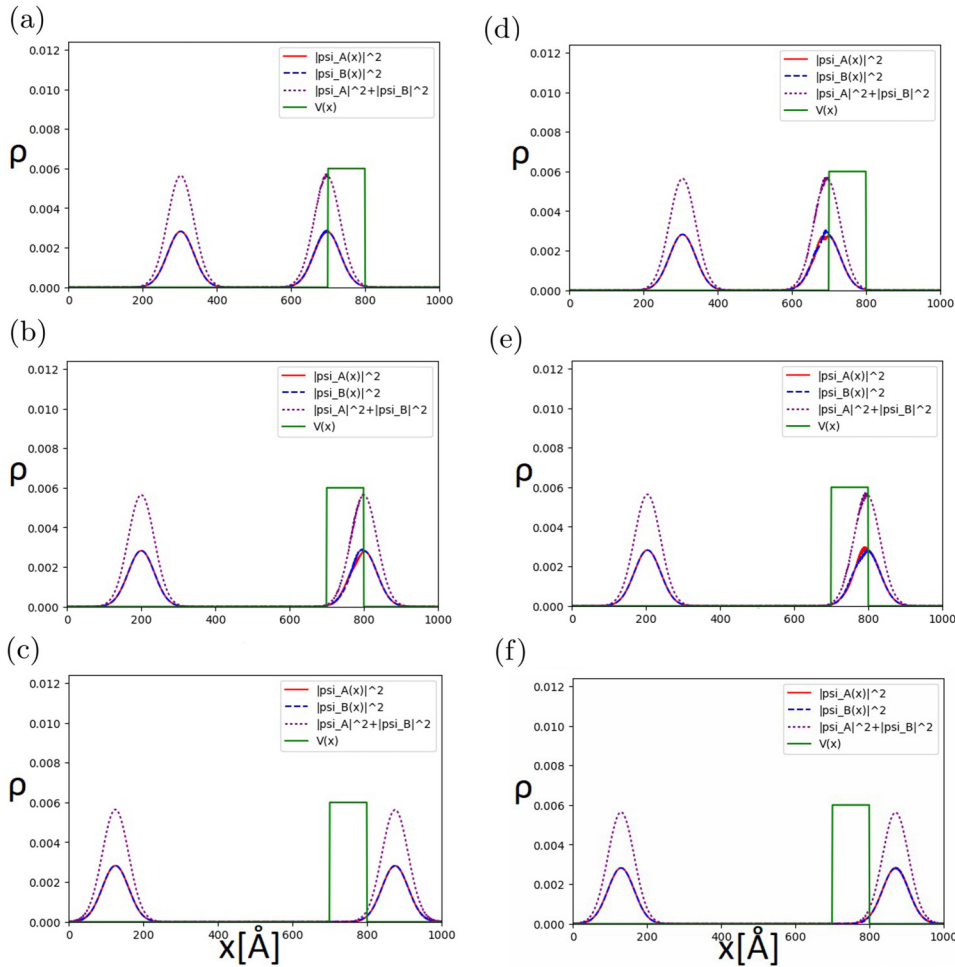
FIG. 7. Klein tunneling. We display a qualitative comparison of the collision with a QB of height $V_0 = 0.3$ eV, thickness $\Delta x_b = 100$ Å, Rashba linear parameter $\alpha = 0.4$ eV Å, and Rashba cubic parameter $\beta = 0.3$ eV Å^3. We have taken $k_x \approx 0$ and $k_y = 0$ (left-column panels) and $k_{x(y)} = 0.09(0)$ Å^{-1} (right-column panels). Panels (a) and (d) display $\rho_{A,B}$ at $t = 25$ fs, when the first interaction of the 1DGWP with the QB occurs, showing almost no change in $\rho_{A,B}$ [panel (a)] and a small ripple in $\rho_{A,B}$ [panel (d)]. Panels (b) and (e) plot at $t = 35$ fs, the second 1DGWP-QB interaction. Though almost imperceptible, each component $\rho_{(B/A)}$ appears slightly above [panel (b)/(e), respectively]. Finally, panels (c) and (f) show the packages at $t = 25$ fs, when they have passed through the QB, without any apparently difference at the box edge.

fermions do not interplay with the SOI-R biased QB in any perceptible way. Meanwhile, when $k_{x(y)} = 0.09(0)$ Å^{-1} (right-column panels), one can see a weak splitting of the 1DGWP when it enters the QB, $|\psi_B|^2$ being slightly above [see the blue-dashed line in panel (d)], otherwise when leaving the QB, it is the component $|\psi_A|^2$ that clearly goes up [see red-solid line in panel (e)]. Even if these differences are quite small, between the cases without PZBE ($k_x \approx 0$ and $k_y = 0$) (see left-column panels of Fig. 5) and with PZBE [$k_{x(y)} = 0.09(0)$ Å^{-1}] (see right-column panels of Fig. 5), the output 1DGWP is the same. The latter has two possible interpretations: (i) From one side, the initial phase contributes to the average velocity,[8] and the incidence angle $\theta = \arctan(k_y/k_x)$ governs the changes in 1DGWP scattering behavior.[32] Then, we conclude that the coordinates of movement we have assumed are those of normal incidence to the QB, because Dirac fermions collide it under $\theta = 0$, for $k_x = 0.09$ Å^{-1} and $k_y = 0$. Thus, Klein's paradox is at play here and the tunneling becomes perfect.[32] (ii) On the other hand, it means that the QB and the SOI-R do not affect substantially the 1DGWP dynamics of the Dirac fermions during their passage throughout the SOI-biased scatterer. Thus, the assessment

of the SOI-R weakness in graphene[3] is now reassured in the study of the PZBE for a Q1D MLG configuration, because the way it gets affected by the SOI-R is so far almost unnoticeable. Pursuing further confirmations, we simulated the dynamics of an identical 1DGWP in MLG quantum wells. We have detected noticeable evidence of the SOI-R modulation on the PBZE that is not shown here, due to the presence of several inconsistencies of the finite-differences method at the box edges, yet to be debugged. This may reopen the belief about the potential existence of an interplay between the ZBE and the SOI-R in graphene, following the dependence of the ZBE on the strength of SOI-R in III–V semiconducting quantum wells.[9]

Figure 8, for the purpose of illustration, exposes an extended sequence of the 1DGWP time evolution inside a 100 Å length surrounding box, to present evidence for a perfect backscattering (anti-Klein tunneling) of the 1DGWP at the QB under SOI-R [see panel (h) and animations of Ref. 31]. On panels (a)–(d), a similar behavior as the one discussed in Fig. 7 (Klein tunneling) can be seen and we have included them for the sake of completeness. Panel (e) plots the first interaction with the QB after the initial
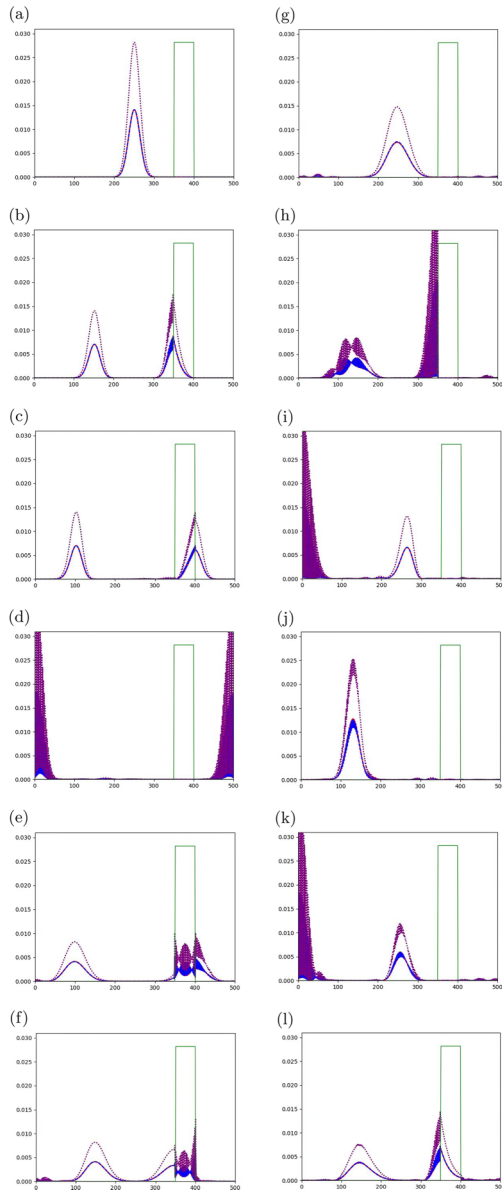
FIG. 8. Anti-Klein tunneling. We show a complete temporal evolution of the WP with $\xi = \begin{pmatrix} 1 \\ i \end{pmatrix}$ colliding with a barrier of height $V_0 = 0.3$ eV, thickness $\Delta x_b = 100$ Å, Rashba linear parameter $\alpha = 0.4$ eV Å, and Rashba cubic parameter $\beta = 0.3$ eV Å^3; with $k_x \approx 0$ and $k_y = 0$. The Klein tunneling of the 1DGWP [panels (a) $t = 0$; (b) $t = 25$ fs, and (c) $t = 35$ fs] as well as its perfect backscattering [panels (g) $t = 100$ fs; (h) $t = 115$ fs, and (i) $t = 135$ fs] can also be seen. In panel (d), we see the 1DGWP colliding at $t = 60$ fs, with the edges of the box, but showing a lot of *cavity noise* due to the complete reflection. Panels (e) $t = 75$ fs and (f) $t = 85$ fs display the third and fourth 1DGWP-QB interactions, respectively. Panel (j) plots the overlap of both halves of the 1DGWP after the perfect backscattering, at $t = 170$ fs. Panel (k) shows both portions of the 1DGWP at $t = 200$ fs, and one can observe that they are no longer Gaussian. This can be better seen in panel (l), when the sixth 1DGWP-QB interaction appears at $t = 225$ fs.

right-hand moving (RHM) sub-1DGWP becomes reflected by the surrounding box wall. Notice some small portions of the sub-1DGWP due to multiple reflections with the QB and the box. They are traveling one way and the other way around at the same time, as they can be disregarded in most of this analysis because they somewhat represent a cavity noise. In panel (f), the backscattered RHM sub-1DGWP is tresspassing the QB moving to the left, while the initial left-hand moving (LHM) sub-1DGWP evolves to the right. Panel (g) shows both sub-1DGWPs overlapped and the noise allocated to both of their sides. Next, on panel (h), there is an appealing total backscattering of the rearranged RHM sub-1DGWP with the QB. For a further understanding of the observed perfect reflection, we recall that ultimately the QB is a resonant cavity, thereby there should exist θ values, for which transmission or reflection maximizes. To support the last point, we assume that unlike massless chiral fermions exhibiting Klein tunneling (conservation of chirality pseudospin index outside-inside the QB),[33] anti-Klein tunneling occurs for chiral fermions with effective mass, due to particles transforming into holes inside the barrier carrying imaginary momenta (nonconservation of chirality pseudospin index outside-inside the QB).[34] We suggest that the SOI-R triggers the precession mechanism of the real spin in the under-QB region, allowing then pseudospin to alternate its chirality index. In the case of the anti-Klein tunneling, which should be suppressed in MLG,[33] by adding a mass-dependent term in the Hamiltonian (7), the pseudospin components of (3) could be coupled, causing the chirality conservation to break.[30] Meanwhile, the LHM sub-1DGWP shape is being distorted by the cavity noise. Panel (i) exhibits the LHM sub-1DGWP collision with the box wall, when the perfect backscattered RHM sub-1DGWP is traveling to the left. On panel (j), they are overlapped one more time, now at the position $x \approx 120$ Å. After this, panels (k) and (l) demonstrate a behavior quite similar to that of panels (a)–(d), except for the sub-1DGWP shape distortion, boosted by the cavity noise. In fact, the perfect tunneling and the perfect backscattering that we found for a Q1D MLG nanoribbon have also been reported recently for 2D MLG.[34] Indeed, the authors find that by tuning a strong SOI-R in 2D MLG, the transmission of Dirac fermions through a potential barrier can start from Klein tunneling and move to anti-Klein tunneling (perfect backscattering). This excellent agreement with the mentioned results,[34] despite several differences between both theoretical modeling and physical setups, shows unequivocally that the proposed device is reliable and our modeling to deal with it correctly captures the essential physical phenomena in MLG systems.

V. CONCLUSIONS

The introduced spintronic device based on a Q1D MLG narrow nanoribbon embedded between a hBN film and a SiO$_2$ insulating substrate is an acceptable workbench that may encourage new experimental directions. The theoretical model we have developed, for describing spin-dependent quantum transport of Dirac fermions confined into the introduced Q1D device, correctly reproduces expected features of prior studies.[8] Most importantly, our main result predicts the pseudospinorial *Zitterbewegung* effect to arise in such Q1D MLG devices. Good qualitative agreement with previous reports of the ZBE in graphene[1,8,13,14] has been achieved, because a

robust transient character of the PZBE oscillations, with a decay time of about 10.5 fs, was found in all cases under examination here. Individual features in graphene electronic devices need to be controlled accurately enough.[16] One of our findings is precisely the demonstration that several features of the PZBE become tunable, even its complete disappearance, as a function of the quasimomentum and the initial pseudospin configuration. Furthermore, when sampling in the vicinity of the Γ and Dirac points, we observed that the frequency of the PZBE and the 1DGWP group velocity depend on their closeness to these high symmetry points. For example, when $k \to \Gamma$, the group velocity $\to 0$, while the frequency maximizes. We do not detect any perceptible influence of the SOI-R on the PZBE features, when the Dirac fermions tresspass the QB. Nonetheless, this assessment is not conclusive yet due to the noticeable modulation of the SOI-R over the PZBE that we observed (to be yet debugged) for multiple quantum wells inside a similar Q1D device. Finally, we have captured evidence of the familiar Klein tunneling and the unusual anti-Klein tunneling, whose interplay for 2D MLG under tunable SOI-R was reported recently.[34] Taking into account all these concrete results, in particular, the last one, we conclude that the proposed device is reliable and our theoretical modeling to deal with it correctly captures the essential physical phenomena in MLG systems.

ACKNOWLEDGMENTS

REFERENCES

[1]J. B. Ming-Hao Liu and K. Richter, Phys. Rev. B **85**, 085406 (2012).
[2]W. Han, R. K. Kawakami, M. Gmitra, and J. Fabian, Nat. Nanotechnol. **9**, 794 (2014).
[3]A. K. Geim and K. S. Novoselov, Nat. Mater. **6**, 183 (2007).
[4]A. H. C. Neto, Rev. Mod. Phys. **81**, 109 (2009).
[5]C. Rodriguez and O. Vasilievna, Ingenierias **11**, 17 (2008); available at http://ingenierias.uanl.mx/38/index.html.
[6]E. Schrödinger, Sitzungsb. Preuss. Akad. Wiss. Phys. Math. Kl. **24**, 418 (1930).
[7]P. Dirac, *The Principles of Quantum Mechanics* (Clarendon Press, Oxford, 1958), pp. 4ff, 253ff.
[8]G. M. Maksimova and E. V. Frolova, Phys. Rev. B **78**, 235321 (2008).
[9]T. Biswas and T. K. Ghosh, J. Appl. Phys. **115**, 213701 (2014).
[10]Q. S. P. Krekora and R. Grobe, Phys. Rev. Lett. **93**, 043004 (2004).
[11]M. I. Katsnelson, Eur. Phys. J. B **51**, 157 (2006).
[12]B. G. Sidharth, Int. J. Theor. Phys. **48**, 497 (2009).
[13]T. Rusin and W. Zawadski, Phys. Rev. B **78**, 125419 (2008).
[14]W. Zawadski and T. M. Rusin, J. Phys. Condens. Matter **23**, 143201 (2011).
[15]H. Min, J. E. Hill, N. A. Sinitsyn, B. R. Sahu, L. Kleinman, and A. H. MacDonald, Phys. Rev. B **74**, 165310 (2006).
[16]A. H. C. Neto, Nat. Mater. **6**, 176 (2007).
[17]M. Ishigami and E. D. Williams, Nano Lett. **7**, 1643 (2007).
[18]S. L. Dong, C. Riedl, B. Krauss, K. V. Klitzing, U. Starke, and J. H. Smet, Nano Lett. **8**, 4320 (2008).
[19]V. Geringer, M. Liebmann, T. Echtermeyer, S. Runte, M. Schmidt, R. Ruckamp, M. C. Lemme, and M. Morgenstern, Phys. Rev. Lett. **102**, 076102 (2008).
[20]J. Wang, F. Ma, and M. Sun, RSC Adv. **7**, 16801 (2017).
[21]K. S. Novoselov, A. K. Geim, S. V. Morozov, D. Jiang, Y. Zhang, S. V. Dubonos, I. V. Grigorieve, and A. A. Firsov, Science **306**, 666 (2004).
[22]A. Young and P. Kim, Nat. Phys. **5**, 222 (2009).
[23]X. L. Z. Qiao, W.-K. Tse, H. Jiang, Y. Yao, and Q. Niu, Phys. Rev. B **87**, 125405 (2013).
[24]A. Varykhalov, J. Sánchez-Barriga, A. M. Shikin, C. Biswas, E. Vescovo, A. Rybkin, D. Marchenko, and O. Rader, Phys. Rev. Lett. **101**, 157601 (2008).
[25]Z. Qiao, H. Jiang, X. Li, Y. Yao, and Q. Niu, Phys. Rev. B **85**, 115439 (2012).
[26]M. Gmitra, S. Konschuh, C. Ertler, C. Ambrosch, and J. Fabian, Phys. Rev. B **80**, 235431 (2009).
[27]C. I. Kane and E. J. Mele, Phys. Rev. Lett. **448**, 226801 (2005).
[28]R. Cuan and L. Diago-Cisneros, Rev. Cub. Fís. **27**, 212 (2010); available at http://www.revistacubanadefisica.org/index.php/rcf/article/view/RCF_27-2B_212_2010.
[29]R. Cuan and L. Diago-Cisneros, Eur. Phys. Lett. **110**, 67001 (2015).
[30]J. M. Pereira, F. M. Peeters, A. Chaves, and G. A. Farias, Semicond. Sci. Technol. **25**, 033002 (2010).
[31]E. Serna, see https://sernaed95.wixsite.com/animaquantrix/animations for multimedia of the 1DGWP wordline dynamic (2018).
[32]H. García-Cervantes, L. M. Gaggero-Sager, O. Sotolongo-Costa, G. G. Naumis, and I. Rodríguez-Vargas, AIP Adv. **6**, 035309 (2016).
[33]M. I. Katsnelson and A. K. Geim, Nat. Phys. **2**, 620 (2006).
[34]L. Dell'Anna, P. Majari, and M. R. Setare, J. Phys. Condens. Matter. **30**, 415301 (2018).